

**Identifying Halos in Cosmological Simulations with Continuous Wavelet Analysis: The 2D Case**MINXING LI (李敏行),<sup>1</sup> YUN WANG (王云),<sup>1</sup> AND PING HE (何平)<sup>1,2</sup><sup>1</sup>*College of Physics, Jilin University, Changchun 130012, P.R. China.*<sup>2</sup>*Center for High Energy Physics, Peking University, Beijing 100871, P.R. China.*

## ABSTRACT

Continuous wavelet analysis is gaining popularity in science and engineering for its ability to analyze data across spatial and scale domain simultaneously. In this study, we introduce a wavelet-based method to identify halos and assess its feasibility in two-dimensional (2D) scenarios. We begin with the generation of four pseudo-2D datasets from the SIMBA dark matter simulation by compressing thin slices of three-dimensional (3D) data into 2D. We then calculate the continuous wavelet transform (CWT) directly from the particle distributions, identify local maxima that represent actual halos, and segment the CWT to delineate halo boundaries. A comparison with the traditional Friends-of-Friends (FOF) method shows that our CWT-identified halos, while containing slightly fewer particles, have smoother boundaries and are more compact in dense regions. In contrast, the CWT method can link particles over greater distances to form halos in sparse regions due to its spatial segmentation scheme. The spatial distribution and halo power spectrum of both CWT and FOF halos demonstrate substantial consistency, validating the 2D applicability of CWT for halo detection. Our identification scheme operates with a linear time complexity of  $\mathcal{O}(N)$ , suggesting its suitability for analyzing significantly larger datasets in the future.

*Unified Astronomy Thesaurus concepts:* [Wavelet analysis \(1918\)](#); [Galaxy dark matter halos \(1880\)](#); [N-body simulations \(1083\)](#); [Large-scale structure of the universe \(902\)](#)

## 1. INTRODUCTION

In modern cosmology, it is assumed that our universe was highly homogeneous in its early stages. Over time, these initial minute density perturbations evolve into a variety of structures, such as dark matter halos, galaxies, clusters, and voids. This evolution occurs through linear and nonlinear processes, driven by long-range gravity (Mo et al. 2010). To study the universe's evolution, observations of astronomical objects at high redshifts and extremely large distances are necessary. These observations are complemented by numerical simulations, which are indispensable tools for cosmological research. Such simulations begin with an initial condition and then solve the  $N$ -body dynamic equations or hydrodynamic equations to simulate the universe's evolution. Within these simulations, the universe's density is represented by particles, typically dark matter and baryonic matter particles, which perform a Poisson sampling of the simulated density field (Peebles 1980).

With the rapid advancement of computer science, cosmological simulations have progressed from simple  $N$ -body

models involving pure dark matter bound by gravity (Press & Schechter 1974) to sophisticated adaptive moving-mesh magneto-hydrodynamic simulations (Nelson et al. 2019) and meshless finite-mass hydrodynamic simulations (Davé et al. 2019), which incorporate processes of feedback and interactions. These advanced simulations enable us to model the evolution of the universe from redshifts of a few hundred to the present day within a simulation box spanning millions or even billions of parsecs in comoving units. While the simulations align with observations in various aspects - such as the existence of cosmic web, the characteristics of stars, and the gas content of galaxies - the analysis of simulated particle data remains challenging. For instance, when determining statistical properties like the power spectrum, particles are commonly assigned to a regular grid using window functions, such as the Count-in-Cell (CIC) or Triangular-Shaped-Cloud (TSC) methods (see Hockney & Eastwood 1981). Moreover, constructing a halo catalog to study the clustering of matter in the simulated universe necessitates identifying individual halos at the particle data limit and considering a cluster of particles as a single halo.

For this purpose, we can employ various halo finders, such as Amiga Halo Finder (AHF) (Knollmann & Knebe 2009), adaptive spherical overdensity halo finder (ASOHF)

(Planelles & Quilis 2010) and ROCKSTAR halo finder (Behroozi et al. 2013), to group particles into a halo. Among them, the most widely used algorithm is Friends-of-Friends (FOF) method (Davis et al. 1985). The FOF method calculates a linking length based on the particle number density and then connects particles whose distance is less than this length. Despite its simplicity, this method is popular for identifying dark halos from particle data due to its ability to provide an accurate measure of halo distribution. However, the FOF method has limitations, in that it has a time complexity of  $\mathcal{O}(N \log N)$  when utilizing a minimal spanning tree for organizing particle data, and it employs an *artificial* parameter  $b$  in the linking length. Worst of all, it does not offer a clear boundary definition, leading to the ‘linking bridges’ problem, where two distinct halos may be erroneously linked if a chain of closely spaced (less than the linking length) particles exists between them (Springel et al. 2001).

In addition to the FOF method, an alternative for analyzing clustering is the wavelet transform method, first introduced by Grossmann et al. (1985). This technique is extensively utilized in astronomy and cosmology to identify structures, such as analyzing clusters in X-ray data (e.g. Vavilova & Babyk 2018; Freeman et al. 2002), infrared data (Wang et al. 2008), and gamma-ray data (Ciprini et al. 2007). It is also used to study how discreteness effects in  $N$ -body simulations affect the statistical diagnostics of the cosmological density field (Romeo et al. 2008), to trace the time evolution of the cosmic web (Einasto et al. 2011), or to identify sunspots (Djafer et al. 2012), and to characterize coronal mass ejections (González-Gómez et al. 2010). Furthermore, the wavelet method is employed to detect Baryon Acoustic Oscillation (BAO) structures (Arnalte-Mur et al. 2012), ridges of spiral arms (Patrikeev et al. 2006), and point source contamination in Cosmic Microwave Background (CMB) observations (Cayón et al. 2000).

There are two distinct wavelet methods, the discrete wavelet transform (DWT) and the continuous wavelet transform (CWT). The DWT decomposes a signal into a set of orthogonal wavelet bases, offering a compact representation. In contrast, the CWT involves the convolution of the signal with a wavelet that is scaled by a mother wavelet. The CWT computation is typically performed on a grid, or image pixels in observations, and uses the Fast Fourier Transform (FFT), exploiting the property that convolution in real space is equivalent to multiplication in Fourier space (e.g. Arnalte-Mur et al. 2012; Grebenev et al. 1995; Barnard et al. 2004; Kazakevich et al. 2004).

In structure identification, the DWT is commonly applied using the ‘à trous’ algorithm, which filters an image with scaling functions at doubled magnification scales and then decomposes it into wavelets at various scales, along with a residual (e.g. Bijaoui & Giudicelli 1990; Pagliaro et al. 1999;

Ellien et al. 2021; Lazzati et al. 1999; Moretti et al. 2004). This algorithm, distinct from the standard DWT, employs a non-orthogonal wavelet basis, enhancing its ability to localize structures (Chereul et al. 1998). It enables rapid computation of grid DWTs at multiple scales with a constant resolution but fixes the scaling to a doubly magnified set of scales.

Compared with the DWT, the CWT typically demands more time and CPU resources for any given data. However, for the discrete particle data encountered in simulations, an alternative method exists to compute the CWT with a time complexity of  $\mathcal{O}(N)$ . This approach views the density field as a sum of Dirac delta functions, which means that the corresponding CWT is the convolution of these Dirac functions with a wavelet, yielding a sum of wavelets. Although some authors describe this method as a DWT (e.g. Bendjoya et al. 1991; Slezak et al. 1993; Flin & Krywult 2006), the outcome of this convolution is inherently continuous, as its value can be determined at any position and scale, irrespective of resolution.

In this paper, we introduce a novel wavelet-based method for two-dimensional (2D) halo identification, visualize the results, and compare them with the traditional FOF method. The paper is organized as follows. In Section 2, we provide a brief overview of the CWT method, the FOF method, the SIMBA data utilized, and the derived pseudo-2D data. Section 3 details our multi-scale CWT halo identification approach. In Section 4, we calculate the statistical significance and investigate the impact of resolution on our method. Section 5 presents our identification findings and compares them with the FOF halo identifications. Finally, we offer conclusions and discuss the implications of our results in Section 6.

## 2. THEORETICAL FOUNDATIONS AND METHODS

### 2.1. The Continuous Wavelet Transform

All the wavelets must meet two criteria: the admissibility condition and the square integrability condition. The former stipulates that the wavelet’s energy must attenuate to zero as the independent variable approaches infinity, while the latter mandates that the integral of the wavelet’s square over the entire space be finite. The CWT is defined as the convolution of the signal  $f(\mathbf{x})$  with a wavelet  $\Psi(w, \mathbf{x})$  (assuming both the signal and the wavelet are real) (Slezak et al. 1990),

$$\tilde{f}(w, \mathbf{x}) = \int_{-\infty}^{\infty} f(\mathbf{u})\Psi(w, \mathbf{x} - \mathbf{u})d\mathbf{u}, \quad (1)$$

where  $\Psi(w, \mathbf{x})$  is a scaled version of the so-called mother wavelet  $\Psi(\mathbf{x})$ , as follows

$$\Psi(w, \mathbf{x}) = w^{d/2}\Psi(w\mathbf{x}), \quad (2)$$

with  $d$  denoting the dimension of space (Wang et al. 2022). In our 2D case, Equation (2) simplifies to

$$\Psi(w, \mathbf{x}) = w\Psi(w\mathbf{x}). \quad (3)$$

We introduce the scale parameter  $w$  instead of the traditional scale indicator  $a$ , with the relationship between them being  $w = 1/a$  (Wang et al. 2022; Wang & He 2022). For discrete particle data from simulations, their density field can be expressed as the sum of the Dirac delta function  $\delta^{(D)}(\mathbf{x})$  located at their positions, weighted by their mass,

$$\rho(\mathbf{x}) = \sum_i m_i \delta^{(D)}(\mathbf{x} - \mathbf{x}_i), \quad (4)$$

where  $m_i$ ,  $\mathbf{x}_i$  represent the mass and position vector of the  $i$ -th particle, respectively. Thus, the CWT of the particle density field is the convolution of the Dirac function with our wavelet, which is simply the translated wavelet itself

$$\begin{aligned} \tilde{\rho}(w, \mathbf{x}) &= \int_{-\infty}^{\infty} \rho(\mathbf{u}) \Psi(w, \mathbf{x} - \mathbf{u}) d\mathbf{u} \\ &= \int_{-\infty}^{\infty} \sum_i m_i \delta^{(D)}(\mathbf{u} - \mathbf{x}_i) \Psi(w, \mathbf{x} - \mathbf{u}) d\mathbf{u} \\ &= \sum_i m_i \int_{-\infty}^{\infty} \delta^{(D)}(\mathbf{u} - \mathbf{x}_i) \Psi(w, \mathbf{x} - \mathbf{u}) d\mathbf{u} \\ &= \sum_i m_i \Psi(w, \mathbf{x} - \mathbf{x}_i). \end{aligned} \quad (5)$$

It is almost impossible to analyse Equation (5) analytically. In this context, we must analyse millions of functions simultaneously (the number of functions equals the number of particles). Instead, we discretize Equation (5) onto a regular grid, that is, we calculate the value of Equation (5) at specific grid points  $\mathbf{x}_g$  to represent it:

$$\tilde{\rho}(w, \mathbf{x}_g) = \sum_i m_i \Psi(w, \mathbf{x}_g - \mathbf{x}_i), \quad (6)$$

which is much more manageable.

In this work, we utilize 2D isotropic Mexican hat (MH) wavelet, defined as

$$\Psi(w, \mathbf{x}) = w(2 - w^2 r^2) e^{-\frac{w^2 r^2}{2}}, \quad (7)$$

which is derived from its mother wavelet

$$\Psi(r) = (2 - r^2) e^{-\frac{r^2}{2}}, \quad (8)$$

where  $r = |\mathbf{x}|$  denotes the magnitude of the vector  $\mathbf{x}$ . This wavelet can be considered, apart from a prefactor, as the first derivative of the Gaussian function with respect to  $w$  (see Wang & He 2021, for details).

Even if we employ isotropic wavelets, they can still be used to detect anisotropic structures (Vavilova & Babyk 2018). To simplify our calculations, we opt for isotropic wavelets with compact support, or at least with an approximate compact support. Furthermore, if a wavelet is not orthogonal, a particular structure might exhibit local maxima at several scales, rather than solely at the scale that most closely matches the

structure's size. This could lead to ambiguity when identifying halos within a multi-scale analysis (Hayn et al. 2012; Ellien et al. 2021). However, it is not feasible for a wavelet to simultaneously possess compact support, isotropy, and orthogonality (Daubechies 1992). Therefore, we select the MH wavelet for its isotropy and approximate compact support (Wang & He 2021). The CWT has a notable property: the CWT of any constant or linear component of a signal is zero. This characteristic provides us with a method to distinguish between different structures, even in highly dense environments, and offers a natural delineation.

## 2.2. Friends-of-Friends Algorithm

The FOF method groups particles into different halos (Davis et al. 1985). The grouping process can be summarized as follows: First, an arbitrary particle is selected. Then search for its nearby particles and links any particle whose distance to the selected one is less than the linking length,  $l_{\text{link}}$ ; these are termed the 'friends' of the initial particle. Subsequently, the search continues for the 'friends' of each newly linked particle. This linking continues to include additional 'friends' whose distance to any current 'friend' is also less than  $l_{\text{link}}$ . The process repeats, finding 'friends of friends', until no new particles can be linked under this criterion. These interconnected particles ultimately form a FOF group.

After that, select another arbitrary particle that is not already in any group and search for its 'friends' to form a new group. Repeat this process until all particles are assigned to groups, even if some groups contain only one particle. Finally, exclude groups that have fewer than a specified threshold number of particles,  $N_{\text{th}}$ ; for example,  $N_{\text{th}} = 5$ . This results in the classification of only those halos that contain five or more particles.

Obviously, there are two artificial parameters in FOF,  $l_{\text{link}}$  and  $N_{\text{th}}$ . The former is usually defined as

$$l_{\text{link}} = b \left( \frac{V}{N} \right)^{1/3}, \quad (9)$$

where  $V$  is the volume of the simulation box,  $N$  is the number of particles, and  $b = 0.2$  so that the average density in the halo is 180 times the average density in the box (More et al. 2011). In the 2D case, Equation (9) can be rewritten as

$$l_{\text{link}} = b \left( \frac{S}{N} \right)^{1/2}, \quad (10)$$

where  $S$  is the area of the simulation box and we still set  $b = 0.2$ . However, the choice for the latter,  $N_{\text{th}}$ , is much

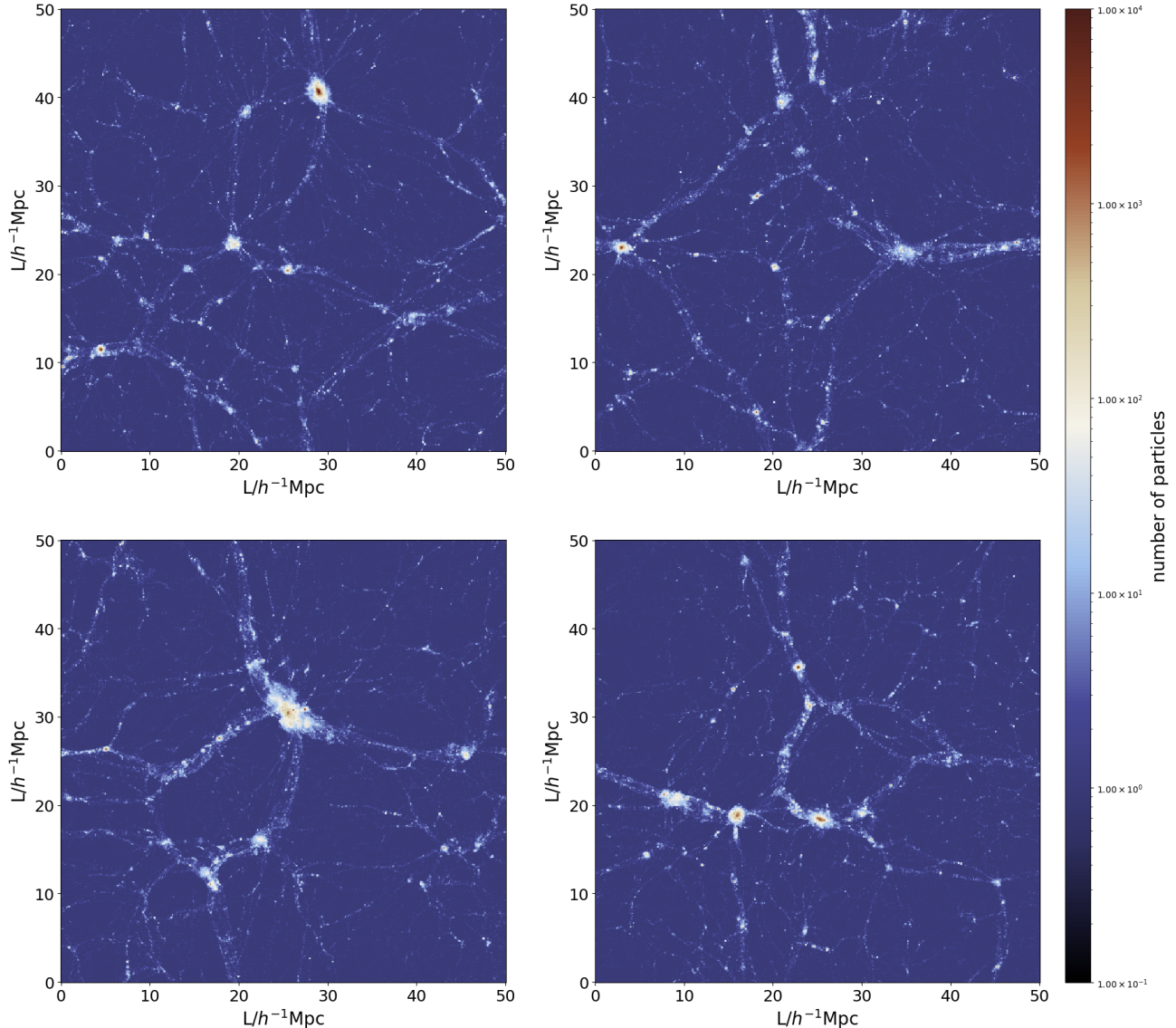


**Figure 1.** The density field of our pseudo-2D data in the CIC grid, from top left to bottom right are slices at  $z = 11.4, 28.4, 38.0$  and  $45.7 h^{-1} \text{Mpc}$ , respectively. The thickness of all the four slices is  $\Delta z = 0.1 h^{-1} \text{Mpc}$ .

more arbitrary. Although  $N_{\text{th}}$  means the mass of the smallest halo, there is no consensual definition<sup>1</sup>.

### 2.3. SIMBA Simulation and Pseudo-2D Data

SIMBA (Davé et al. 2019) is a meshless finite mass hydrodynamic cosmological simulation based on the GIZMO cosmological gravity plus hydrodynamics solver (Hopkins 2015), assuming  $h = 0.68$ ,  $\Omega_{\Lambda} = 0.7$ ,  $\Omega_{\text{m}} = \Omega_{\text{dm}} + \Omega_{\text{b}} = 0.3$ ,  $\Omega_{\text{b}} = 0.048$ ,  $n_{\text{s}} = 0.97$  and  $\sigma_8 = 0.82$ , which are the Planck cosmological parameters (Planck Collaboration et al. 2016). This simulation consists of several sub-simulations

with different box lengths, particle numbers and even different physics, e.g. no AGN, no jet and pure dark matter.

The purpose of this paper is to identify halos from particle data, without delving into the detailed physics of the simulation. We therefore use the m50n512 dark matter sub-simulation, which is a pure dark matter run without any complicated processes such as star formation, gas cooling, feedback and so on. This sub-simulation has a box length of  $50 h^{-1} \text{Mpc}$  and contains  $512^3$  dark matter particles.

To obtain 2D data, we select the snapshot of redshift  $z = 0$  from this sub-simulation and cut a slice in the  $z$ -direction, and keep only the  $x$ -,  $y$ -coordinates of these particles. This is actually pseudo-2D data with the dimension reduced from the original three-dimensional (3D) data, but it still contains

<sup>1</sup> Someone authors set  $N_{\text{th}} = 32$  (see [http://swift.dur.ac.uk/docs/FriendsOfFriends/algorithm\\_description.html](http://swift.dur.ac.uk/docs/FriendsOfFriends/algorithm_description.html)), while others have different definitions (e.g. yastastro toolkit has the default  $N_{\text{th}} = 5$ ) (Turk et al. 2011).

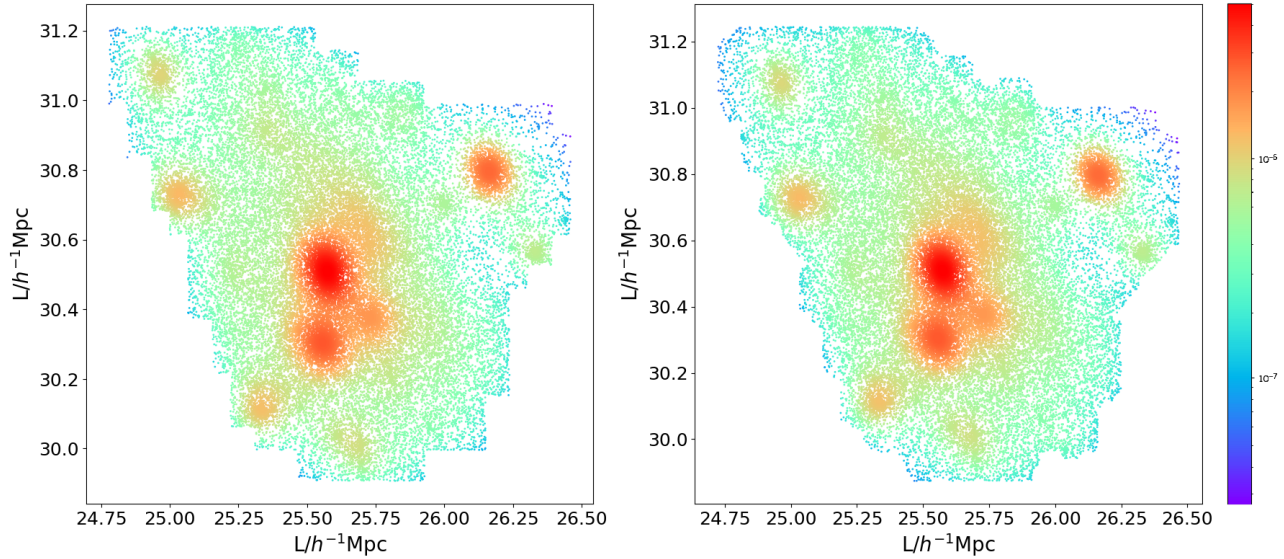


**Figure 2.** The same halo is depicted with directly assigned particles (left) and weighted assigned particles (right). The halo assigned directly exhibits a very sharp boundary, whereas the weighted assignment results in a much smoother boundary.

a lot of structures and is sufficient to test our identification algorithm.

We use four slices of pseudo-2D data at  $z = 11.4$ , 28.4, 38.0 and  $45.7 h^{-1} \text{Mpc}$  with a thickness of  $\Delta z = 0.1 h^{-1} \text{Mpc}$ , containing 323,716, 228,187, 303,692 and 312,372 particles, respectively. The CIC grid of these slices are shown in Figure 1.

### 3. HALO IDENTIFICATION

#### 3.1. Procedure of Identification

We provide a detailed description of our halo identification algorithm, which consists of the following steps:

(1) Calculation of the grid CWT at different scales using a grid-assigning method, as shown in Equation (6), results in an  $\mathcal{O}(N)$  time complexity.

(2) Determination of thresholds to filter those local maxima generated by Poisson noise at different scales, as discussed in Section 3.3, is performed using either the Monte Carlo method or a pre-calculated empirical formula.

(3) Identification of local maxima in the CWT that exceed the threshold at each scale, followed by a comparison across scales to ensure that only the largest CWT value remains at any given location.

(4) Preservation of these local maxima is accompanied by the segmentation of the grid CWT at each scale, with boundaries defined by grid points that are less than or equal to zero and exhibit a decreasing CWT value, which naturally delineates the halo's boundary.

(5) Evaluation of each maximum to confirm its location within a structure at its corresponding scale, discarding any structure that lacks a maximum.

(6) Utilizing the zoom function from `scipy.ndimage`, adjust the resolution of these structures and their backgrounds to a common level and overlay them in descending order of scale size. When two structures overlap, retain only the structure originating from the larger scale. The structures that remain represent potential halos.

(7) Verification of each particle's position within a structure is conducted; if confirmed, the particle is labeled with the index of the potential halo. After all particles have been verified, any halo containing too few particles is discarded.

In the following, we present the detailed calculations for each step of the process.

#### 3.2. Grid-based CWT Computation

In Equation (6), we have derived that the grid CWT is the sum of the wavelets centered on the position of the particles. Since the MH wavelet  $\Psi(x)$  in Equation (8) has an approximate compact support, it affects only a finite range near its center. For some  $r_c > 0$ , if  $|\Psi(|\mathbf{x}| > r_c)|$  is less than, say,  $10^{-10}$ , then we can truncate  $\Psi(|\mathbf{x}| > r_c)$  to be zero. This property allows a convenient calculation of the grid CWT, since a wavelet of a given scale will only have a non-zero value at grid points near its center.

We divide the simulation box into a  $N_g^2$  grid and consider only  $N_W^2$  grid points for each wavelet. The parameters are defined as follows:

$$N_g = \text{Int}(1000 \times k_w) + 500,$$

$$N_W = \text{Int}(2 \times (10/k_w + 10)) + 1,$$

where we introduce the dimensionless scale parameter  $k_w$ , which is expressed in terms of the length of the simulation

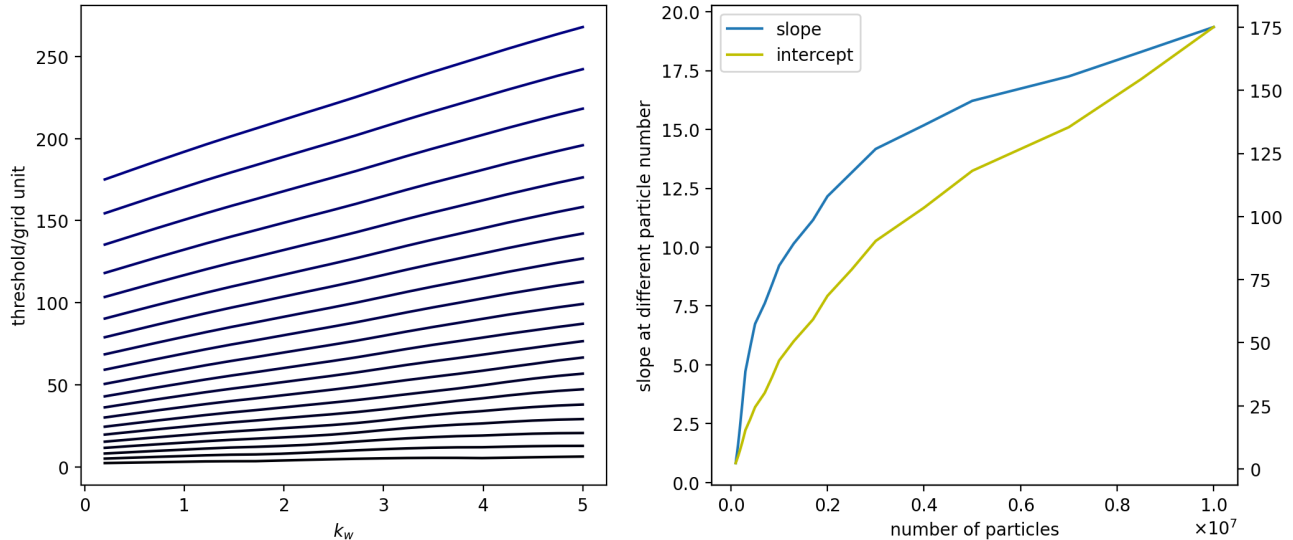


**Figure 3.** Left: Threshold- $k_w$  relationship at different particle numbers, ranging from  $N = 10^5$  (bottom, black) to  $10^7$  (top, blue). We can observe that the relationship between the variables demonstrates high linearity. Right: The slope and intercept of the linear relation from the left panel are shown as functions of the particle number.

box  $L_{\text{box}}$  as

$$k_w = \frac{L_{\text{box}}}{1000} w. \quad (11)$$

In this way,  $k_w = 1$  always represents an intermediate scale when identifying halos, and for the current work,  $k_w = 1$  corresponds to a scale factor of  $20 h\text{Mpc}^{-1}$ . A dynamic mesh is created based on the variable  $k_w$  to save memory and speed up computation. To accurately compute these translated wavelets on the grid, the grid point closest to the position of the particle is selected as the center of the grid wavelet, and this grid point is extended by  $\text{Int}(10/k_w) + 10$  grid points in each direction. We will discuss the resolution parameters in the above two equations in detail in the next section.

The  $N_g^2$  grid is initialized with zeros, and each individual CWT, corresponding to its particle in the  $N_W^2$  grid, is calculated and added to the appropriate part of the  $N_g^2$  grid. This part is centered at the grid point nearest to the particle and extends  $\text{Int}(10/k_w) + 10$  grid points in each direction. If a particle is located near the edge of the simulation box, its extended  $\text{Int}(10/k_w) + 10$  grid points may overflow beyond the  $N_g^2$  grid. In this scenario, the overflowed grid points is moved to the opposite side, using the periodic boundary condition applied to the particle data.

### 3.3. Cross-Scale Analysis of Local Maxima and Thresholding

After calculating the CWT grid, the clustering of particles can be easily analyzed (Slezak et al. 1990). When using wavelets to identify haloes, it is generally agreed that each halo should be located at the position of its corresponding

local maximum. The scale at which we find the maximum represents the size of the structure (e.g. Bendjoya et al. 1991; Flin & Krywult 2006; Grebenev et al. 1995; Slezak et al. 1993; Cayón et al. 2000; Lazzati et al. 1999; Patrikeev et al. 2006; Hayn et al. 2012). Since our wavelet is not orthogonal, finding its local maximum directly in 3D space (2D location plus 1D scale parameter) can be misleading, as a single structure may reach its maximum at multiple scales (Hayn et al. 2012; Ellien et al. 2021). Therefore, we need to check these maxima across scales to ensure that we identify the maximum that corresponds to the actual structure, that is, the largest maxima near the position of this structure.

Also, the particle distribution represents a Poisson sampling of the so-called real density field, which introduces Poisson noise that can lead to spurious local maxima when calculating the CWT using these particle data (Bijaoui et al. 1992). To mitigate this issue, a significance test should be conducted to assess the likelihood of detecting the true structure as opposed to Poisson noise. We apply thresholds obtained from Monte Carlo simulations and eliminate any maxima that do not meet these thresholds across each scale. A detailed description of this process will be presented in the subsequent section.

Once we have identified all thresholded local maxima, we divide the simulation box into an additional set of the  $N_{\text{cs}}^2$  grid for cross-scale comparison. Our cross-scale comparison is based on a grid approach, not only because of the non-orthogonality of the wavelet but also due to the use of a dynamic mesh. The introduction of the new  $N_{\text{cs}}^2$  grid provides a consistent spatial resolution across scales, rather than varying resolutions.

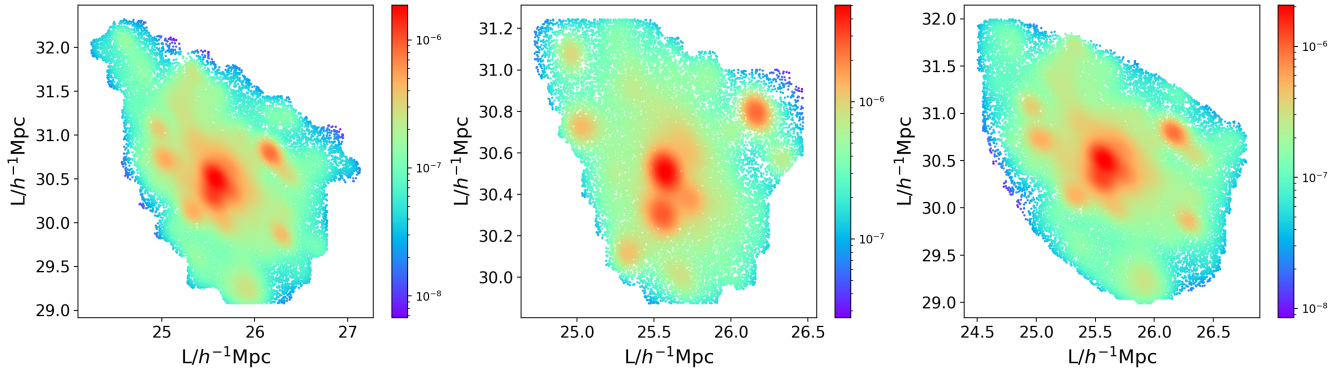


**Figure 4.** The largest halo within the slice at  $z = 38.0 h^{-1} \text{Mpc}$ , presented from left to right at low ( $500 \times k_w + 250$ ), medium ( $1000 \times k_w + 500$ ), and high ( $2000 \times k_w + 1000$ ) resolutions.

We then convert the location of these maxima, which is expressed as the count of grid lengths at their corresponding scale, to the position on the  $N_{\text{cs}}^2$  grid, starting from the larger scale to the smaller scale (from a smaller  $w$  to a larger  $w$ ). When we map a maximum onto the  $N_{\text{cs}}^2$  grid for cross-scale comparison, we compare its CWT value with the values of the surrounding  $3 \times 3$  grid points centered on the grid point of this maximum. If this maximum has a higher CWT value than all nine values within the surrounding grid points, we clear the information stored in those nine grid points and record the information of this maximum in its corresponding grid point. This ensures that there is only one maximum with the highest CWT value within every  $3 \times 3$  grid block of the  $N_{\text{cs}}^2$  grid. These maxima correspond to halo candidates in our method.

### 3.4. Grid Segmentation and Halo Boundary Delineation

To identify a halo, a clear boundary must be established between the halo and the background universe. Fortunately, the wavelet method provides a natural boundary through its inherent properties. If the signal's shape is consistent with that of the wavelet, such as at the peak of the signal, then a positive CWT value is obtained in that region. Conversely, if the signal shape is opposite to the wavelet, such as at the valley of the signal, then a negative CWT value is obtained in that region. Besides that, the matching between the peak and the negative ring of our wavelet also leads to negative CWT value (see Figure 5). No doubt, the positive CWT value inside the peak, while the negative CWT value, where the peak and the negative ring matches, outside the peak. If a wavelet matches with a peak in a positive signal, that means the positive part has the similar size as the peak, leaving the negative ring outside. In this way, points where the CWT equals zero is an intermediate position and serve as the boundary of the peak in the CWT field. However, since the CWT is calculated on a finite grid, finding the grid points where the CWT equals zero can be insufficient. In some cases, there may not be any grid points that are strictly equal to zero.

Fortunately, we can also use all the outer regions as boundaries to isolate halos. This allows us to segment the full CWT grid at each scale into ‘islands’ of positive values surrounded by a ‘sea’ of zero or negative values. These ‘islands’ represent clusters at that scale. Similar segmentation methods have been employed in many previous studies to identify various structures within the CWT grid (e.g. [Baluev & Rodionov 2020](#); [Freeman et al. 2002](#)), as well as in the DWT grid (e.g. [Pagliaro et al. 1999](#); [Mertens & Lobanov 2015](#)).

This method is effective for small and medium scales, but it is not suitable for large scales. The support of wavelet is more extensive at larger scales, which results in the linking of nearby structures by ‘positive bridges’. Additionally, the lower grid resolution at larger scales exacerbates this situation. Regardless of the constant boundary condition applied, some structures are invariably linked by a ‘positive bridge’.

Despite its substructures, a gravity-bound halo exhibits a unimodal structure. At a larger scale, these substructures have a negligible impact on the CWT. Therefore, any actual halo must have a unimodal CWT. With this in mind, we introduce a new boundary condition akin to that described in ([Freeman et al. 2002](#)), which divides closely situated structures by identifying the saddle point between them. At any scale, we start by identifying all local maxima in the CWT and use these as the basis for initial segmentation. During each iteration, we examine all connected grid points to determine if any are lower than their connected structure grid points yet higher than zero. We then expand these structures to include neighboring grid points that meet the aforementioned criteria. The expansion of structures continues until no neighboring grid points can be incorporated. At that point, our segmentation process is complete.

As mentioned in Section 3.3, a single structure can generate multiple ‘islands’ across various scales. Therefore, it is necessary to associate each halo candidate maximum with an ‘island’ to prevent multiple detections. Additionally, substructures must be excluded, as they can also correspond to local maxima and ‘islands’, which can lead to confusion

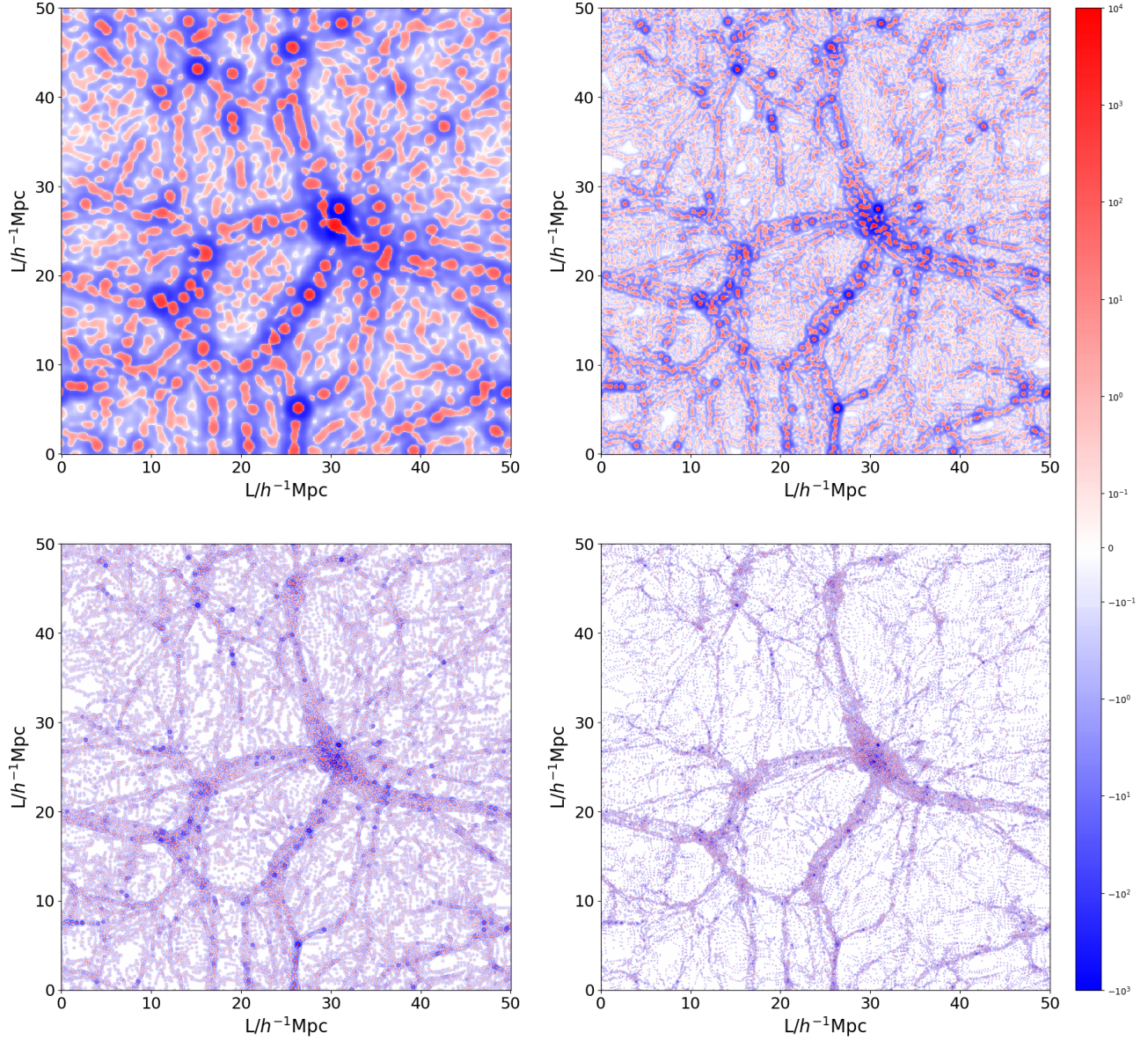


**Figure 5.** The 2D CWT of the slice of  $z = 38 h^{-1} \text{Mpc}$  with four different scales, ranging from  $2.29 h \text{Mpc}^{-1}$  to  $35.24 h \text{Mpc}^{-1}$ . The sizes of the structures presented in these CWTs vary depending on the scale parameter, extending from large to small scales.

when identifying halos. We zoom in on all the ‘islands’ and their corresponding background ‘sea’ at different scales to the highest resolution, which is the resolution of the smallest scale factor  $w$ . Every halo candidate is then assessed from larger to smaller scales. If a halo candidate is located within an ‘island’ at its scale and this ‘island’ does not overlap with any confirmed structures, it is registered as a halo.

### 3.5. Refinement and Smoothing of Halo Boundaries

After registering all halos on a map with the highest resolution (smallest scale), we examine each particle to determine if it is located within a halo and label it with the corresponding halo index. However, due to our limited grid resolution, the CWT halo in the densest regions has very sharp edges.

To address this issue, we propose checking if the particle is located within any particular halo grid, as shown in left panel of Figure 2. To prevent sharp edges, we examine the halo attribution of the four nearest grid points for each particle and calculate the particle’s weight to the four grid points using a CIC weighting formula, as

$$q_{i,j} = (1 - x_i)(1 - y_j), \quad (12)$$

where  $x_i, y_j$  represent the normalized distances to the  $i, j$ -th grid in  $x$ - and  $y$ -direction, respectively, and  $i, j \in [1, 2]$  denote the four nearest grid points. After obtaining the weights, we sum them up if some grid points are assigned to the same halo. The particle is then assigned to the halo with the largest weight (we consider the background as halo ‘0’). From Fig-

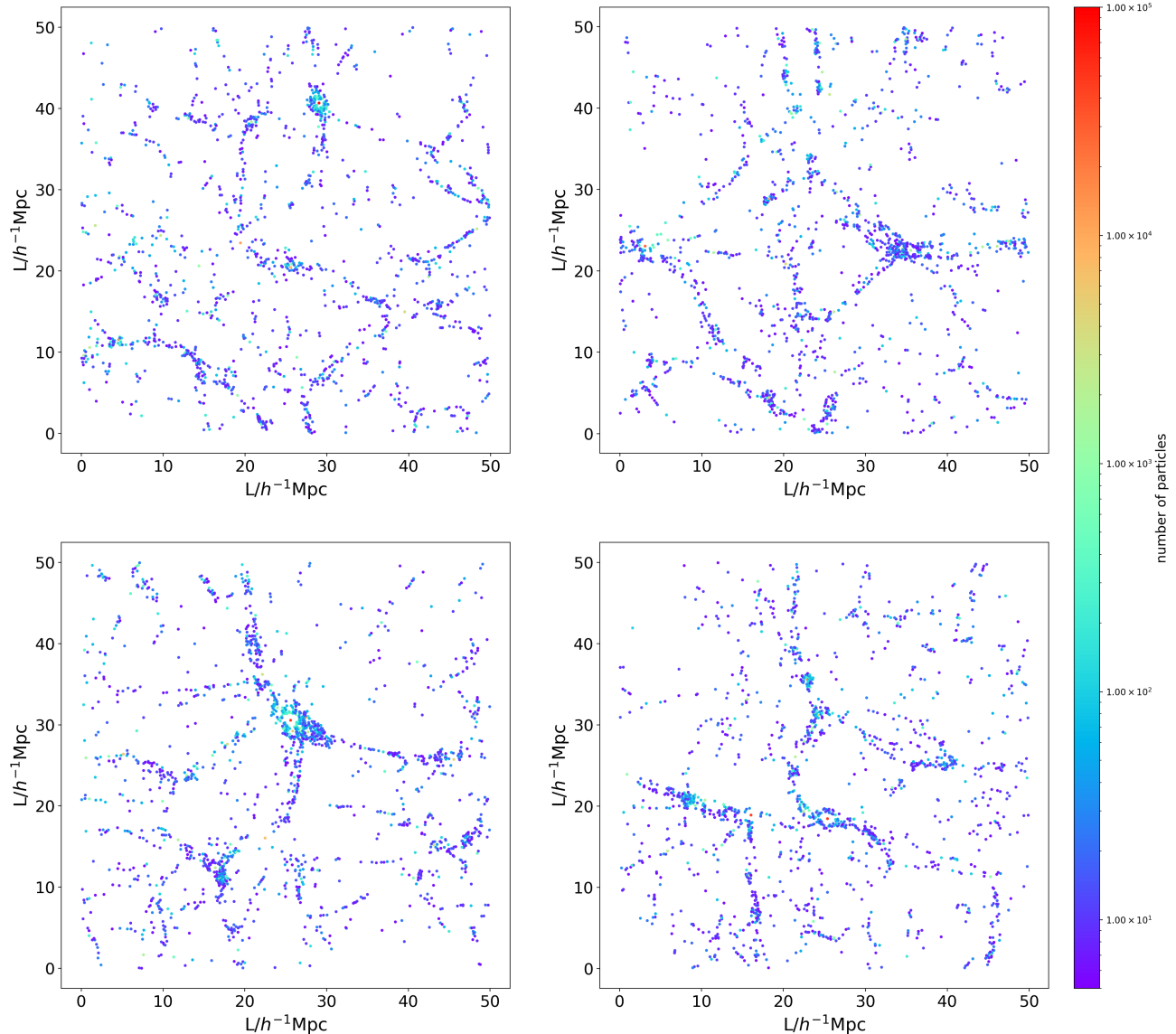


**Figure 6.** The CWT halos of our pseudo-2D data. The slices are arranged in the order of  $z = 11.4, 28.4, 38.0$  and  $45.7 h^{-1} \text{Mpc}$  from top left to bottom right.

ure 2, we can see that after weighting, the previously sharp edges are now smoother. Nevertheless, even with the implementation of our smoothing strategy, the CWT halo exhibits numerous sharp edges due to the limited resolution. Finally, we discard halos that contain too few particles and obtain our final identification result.

#### 4. SIGNIFICANCE AND RESOLUTION

##### 4.1. Determining Significance Levels and Threshold Criteria

In the previous section, we applied thresholding to the local maxima due to the presence of Poisson noise. The CWT of a uniform density field should ideally be zero, but the representation of the true density field using finite particles constitutes a Poisson process. This process leads to fluctua-

tions in the CWT values, resulting in the generation of maxima and minima. Principally, there are two distinct methods to calculate the threshold when identifying structures using wavelets: one is based on the standard deviation of the data (e.g. Grebenev et al. 1995; Lazzati et al. 1999; Cayón et al. 2000; Barnard et al. 2004, and others), and the other employs Monte Carlo simulation (e.g. Bijaoui et al. 1992; Flin & Krywult 2006; Pagliaro et al. 1999; Kazakevich et al. 2004). In this paper, we adopt the Monte Carlo method, as it allows us to pre-calculate the threshold for various cases. This approach yields an empirical formula that significantly simplifies the identification process.

The concept of employing random simulation to assess significance was initially introduced by (Bijaoui et al. 1992). This approach was subsequently adopted by (Slezak et al.

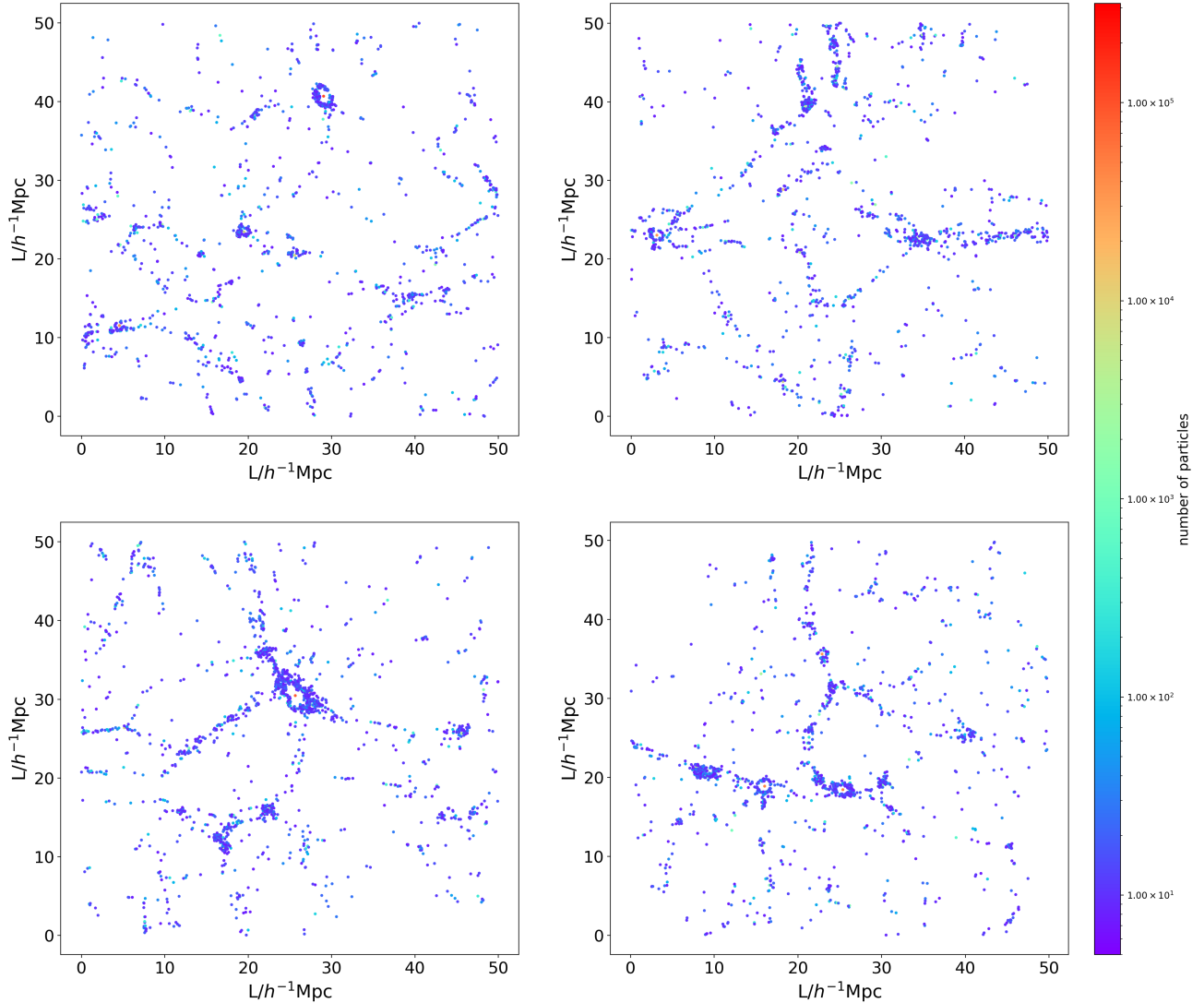


**Figure 7.** Same as Figure 6, but these halos are derived using the FOF method.

1993; Escalera et al. 1994) for the identification of structures using wavelets. The likelihood of identifying a spurious structure post-thresholding is termed the significance level. To evaluate the threshold, we can create a uniform Poisson noise ensemble that mirrors our data in particle count, as this noise originates from a Poisson process. It is crucial to recognize that each local maximum within the noise corresponds to a potential false structure. Consequently, following thresholding, any surviving grid points could result in a false identification. Therefore, the probability of a false identification, also referred to as the significance level, can be estimated by determining the proportion of CWT values that surpass the threshold.

To determine these thresholds, we conducted 800 iterations of Monte Carlo simulations at each scale, averaging the thresholds at a significance level of 0.005. Running Monte Carlo simulations each time we identify halos is time-

consuming and computationally intensive. The threshold is dependent solely on the dimensionless scale parameter  $k_w$  and the number of particles, assuming the resolution remains unchanged. Hence by performing Monte Carlo simulations for a specified resolution and across a wide range of values for both the particle number and  $k_w$ , we can derive an empirical formula. This formula will facilitate future halo identification processes.

We find that for any given particle number  $N_p$ , our threshold grows linearly with  $k_w$  (see left panel of the Figure 3). Thus, we assume our empirical formula has the following form:

$$TH(k_w, N_p) = k(N_p) \times k_w + b(N_p), \quad (13)$$

where  $k$ ,  $b$  represent the slope and intercept of the linear function, respectively, and both are solely dependent on  $N_p$ . From the right panel of Figure 3, the slope and intercept can

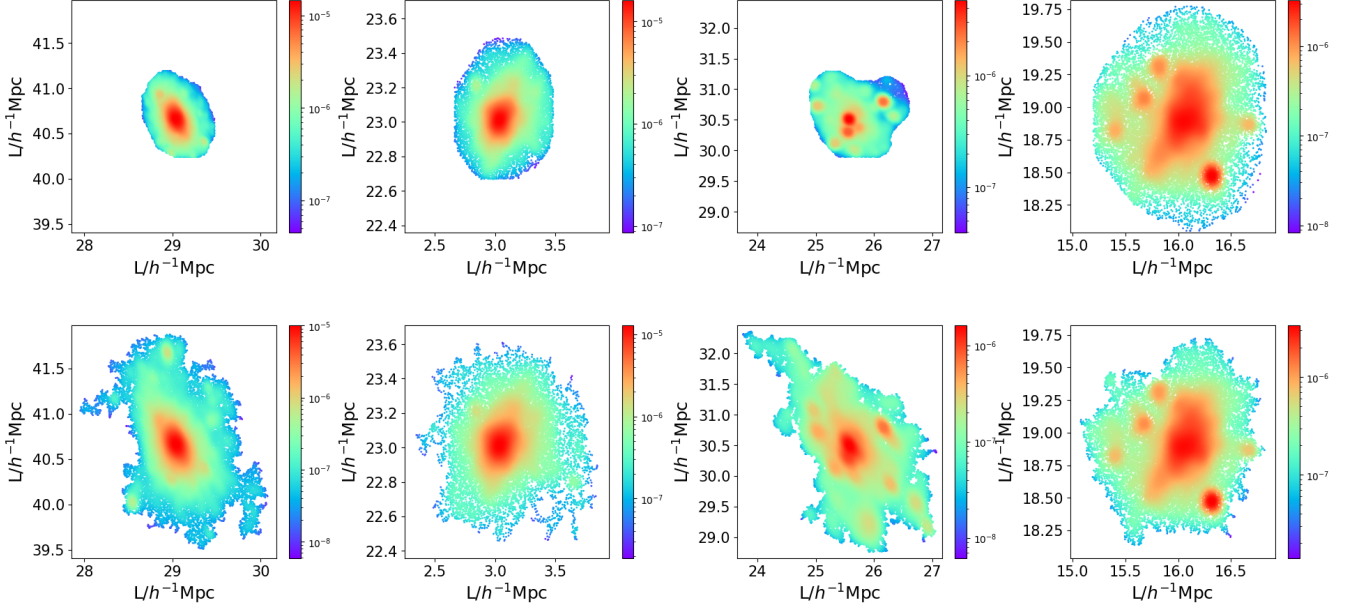


**Figure 8.** The largest halos in the four slices are identified by the CWT (top) and the FOF (bottom) methods. All particles within these halos are scattered and are colored according to their local density.

be fitted with a cubic function. Consequently, our empirical formula takes the following form:

$$TH(k_w, N_p) = k(N_p) \times (k_w - 0.2) + b(N_p), \quad (14)$$

where

$$k(N_p) = 3.0449 \times 10^{-18} N_p^3 - 1.3225 \times 10^{-11} N_p^2 + 1.9170 \times 10^{-5} N_p - 0.8680,$$

$$b(N_p) = 6.2348 \times 10^{-18} N_p^3 - 3.1443 \times 10^{-11} N_p^2 + 7.0298 \times 10^{-5} N_p - 4.3582.$$

Equation (14) is valid within the range  $0.1 < k_w < 5$  and  $10^5 < N_p < 3 \times 10^6$ , exhibiting an approximate dispersion of 10%. As  $k_w$  increases, the support of each particle seldom intersects, causing the threshold to decrease with larger  $k_w$  and to deviate from the linear relationship in scenarios with fewer particles.

#### 4.2. Optimal Grid Resolution for Accurate Halo Representation

To accurately represent the original CWT with a finite grid, it is preferable to sample the CWT on a grid that is not too sparse, given its approximate compact support. Each grid point can only sample particles within a finite area centered on the grid point. However, increasing the density of the grid points significantly increases computational costs. Therefore, we tested three sets of different resolutions:

$$N_{g,h} = \text{Int}(2000 \times k_w) + 1000,$$

$$N_{W,h} = \text{Int}(2 \times (10/k_w + 20)) + 1,$$

for high Resolution,

$$N_{g,i} = \text{Int}(1000 \times k_w) + 500,$$

$$N_{W,i} = \text{Int}(2 \times (10/k_w + 10)) + 1,$$

for intermediate resolution, and finally, for low resolution, we set

$$N_{g,l} = \text{Int}(500 \times k_w) + 250,$$

$$N_{W,l} = \text{Int}(2 \times (5/k_w + 6)) + 1.$$

We depict the same largest halo in a  $38 h^{-1}\text{Mpc}$  slice across different resolutions to illustrate the resolution effect in Figure 4. We identified 1,059, 1,673, and 1,257 halos containing 164,885, 180,834, and 183,772 particles, respectively, from low to high resolution. For the largest halo, the low and high resolution images contain more particles (77,695 and 80,615) than the medium resolution (49,599), resulting in a lower count of halos detected in their runs. The low-resolution and high-resolution images exhibit a more elongated shape, whereas the medium-resolution image appears more compact. All three figures represent the same halo, and without a doubt, the high-resolution image provides the smoothest boundary.

As defined in Section 3.3, the true structure corresponds to the largest CWT maxima across scales. So in both high-resolution and low-resolution runs, the largest halo is incorrectly selected due to the shift of the local maxima. Our cross-scale comparison is based on the positions of these maxima. If a maximum falls outside of our comparison range, it will still be considered valid, even if it does not accurately represent the true scale of the structure. The CWT

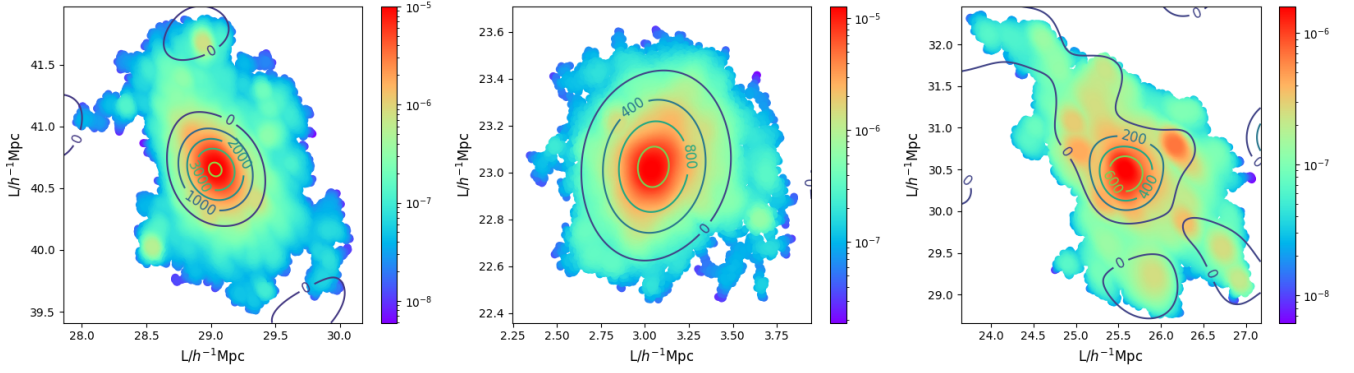


**Figure 9.** The three largest FOF halos from the slices  $z = 11.4, 28.4,$  and  $38 h^{-1}\text{Mpc}$  are shown, along with their CWT contours. In dense regions, the CWT halo excludes the outermost parts of the FOF halo.

maxima value of structures shown in the left panel and right panel of Figure 4 only reaches approximately  $200 h^{-1}\text{Mpc}$ , while the value of the true cross-scale CWT maxima is larger than  $400 h^{-1}\text{Mpc}$ .

Increasing the grid resolution typically separates closely linked structures that are obscured by low spatial sampling. However, in this particular case, doubling the resolution leads to the inclusion of even more particles in the largest halo, which is comparable to a FOF cluster containing 86,331 particles. What’s more, the shift of maxima causes the selection of larger structure as halo, which leads to a decrease in halo number. To prevent the halo from becoming excessively large and to reduce computational costs, we ultimately chose the intermediate resolution. At this resolution, we sample each individual CWT - specifically, just the MH wavelet itself - using more than 400 grid points within its support. This approach allows for an accurate representation of the CWT’s shape. Additionally, as can be seen from Figure 9, with a sufficiently high grid resolution, the intermediate image’s boundary most closely matches the true boundary.

## 5. RESULTS

As previously mentioned, the clustering information is well-preserved in the CWT of the density field, as shown in Figure 5. This figure presents four different CWTs for the slice at  $z = 38.0 h^{-1}\text{Mpc}$ , covering scales from large to small. Notably, all four CWTs exhibit a spatial distribution similar to that of the CIC density. Higher densities in the density field also result in higher CWT values, while the absence of particles corresponds to a CWT value approaching zero. Additionally, every positive clump in the CWT is encircled by a high-negative ring caused by the matching of the negative ring of the wavelet and the density peak, which is the boundary of these clumps in our definition.

The figures confirm the ability of the CWT to distinguish structures across scales. The CWT at a larger scale contains larger clumps, and as the scale parameter increases (towards

**Table 1.** The properties of FOF halo and CWT halo in our four slices.

Halo source	Total particles	Halo number	Largest halo size
FOF114	233,211	1,340	119,445
CWT114	209,959	1,494	89,814
FOF284	142,777	1,318	33,133
CWT284	128,030	1,492	27,692
FOF380	196,385	1,801	86,331
CWT380	180,834	1,673	49,599
FOF457	221,206	1,489	47,061
CWT457	202,535	1,545	46,596

NOTE—In ‘Halo source’, FOF114 and CWT114 denote the FOF and CWT halos, respectively, from the slice at  $z = 11.4 h^{-1}\text{Mpc}$ . Other data are named in a similar fashion. ‘Total particles’ indicates the overall number of particles within halos. ‘Halo number’ signifies the count of halos listed in these catalogs. ‘Largest halo size’ refers to the number of particles contained within the largest halo.

a smaller physical scale), the size of these clumps decreases. The CWT at any given scale reflects the clustering of particles into clumps at a size corresponding to this scale, and the value of the CWT represents the amplitude or strength of its corresponding clump.

Figures 6 and 7 present the distribution of our CWT halos and their corresponding FOF halos. The dimensionless scale parameter  $k_w$  ranges from 0.05 to 2, corresponds to a physical scale of  $1 h^{-1}\text{Mpc}$  to  $0.025 h^{-1}\text{Mpc}$  when identifying halos. The structures of the FOF and CWT halos are similar and consistent with the CIC grid. However, the CWT halo exhibits a significantly more abundant structure. Additionally, there are more CWT halos in the medium mass range, containing 10 – 100 particles (represented by cyan to baby blue

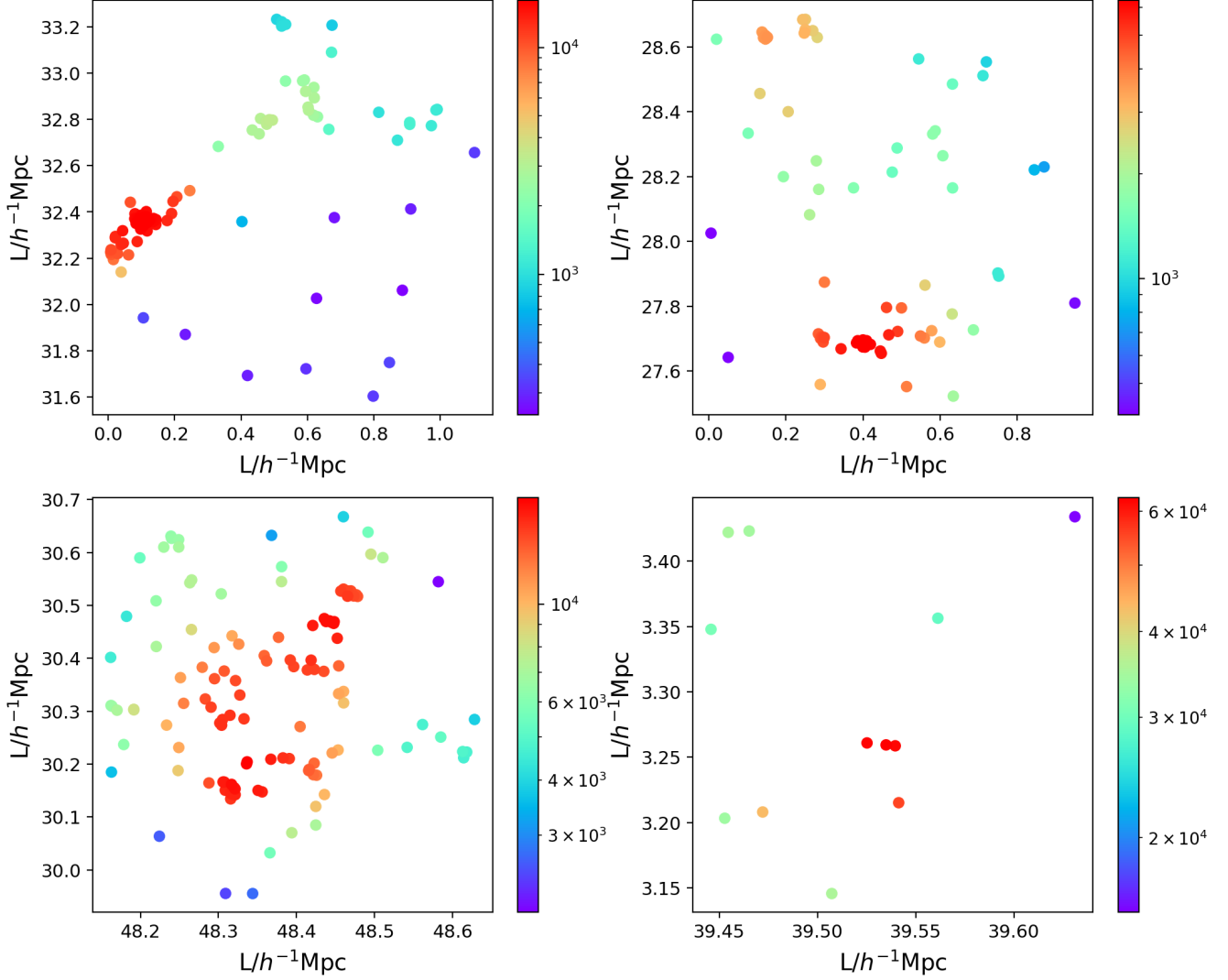


**Figure 10.** Four individual CWT halos from the slice of  $z = 38.0 h^{-1} \text{Mpc}$ , and the linking length in this slice is  $0.018 h^{-1} \text{Mpc}$ . We can easily recognize that these particles would not be linked as a whole halo using the FOF method.

in the colormap), than there are FOF halos. For the smallest halos (represented by blue to purple in the colormap), FOF halos are predominantly found in a higher mass range of approximately 10 particles (dark blue in the colormap), whereas the CWT halos encompass a smaller number of particles (purple in the colormap). Furthermore, there are some isolated red points in dense regions that correspond to very large halos in both FOF and CWT.

The detailed comparison between the FOF halo and the CWT halo are summarized in Table 1. The FOF method accounts for approximately 70% or less of the total particles, while the CWT accounts for over 60% of the particles. Specifically, the CWT method identifies halos containing 10% fewer particles in total and has a slightly higher number of halos compared to the FOF method. Moreover, the largest FOF halo contains approximately 30% more particles on average than that of CWT halo.

When focusing on the densest regions, it is evident that the largest CWT halos are consistently surrounded by several intermediate-mass halos containing a few hundred particles. In contrast, the neighborhood of the largest FOF halo contains fewer particles, even in the final slice where the largest CWT and FOF halos are nearly identical. The discrepancy is primarily attributable to the compact shape of the CWT halo, although it is likely that the ‘linking bridge’ problem inherent in the FOF method also contributes. In dense regions, the high particle density promotes the formation of a chain of particles that links two nearby halos, resulting in a larger halo.

Figure 8 presents the largest halos identified by the FOF method and their corresponding CWT halos. Each point represents a particle within this halo, and its color corresponds to the local density. These halos share similar positions and shapes, suggesting that they can be considered as the same

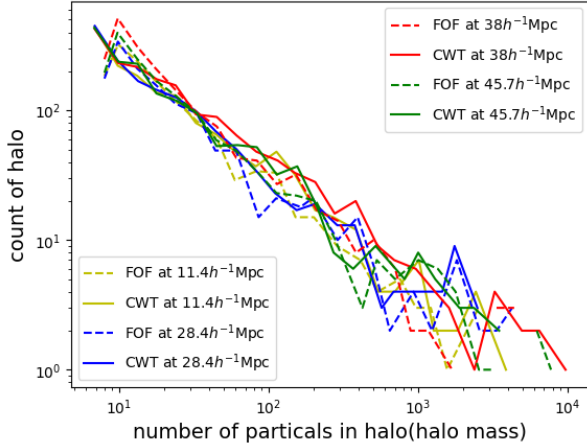


**Figure 11.** Halo mass function across four slices: the solid line represents the mass function of the CWT halos, and the dashed line represents that of the FOF halos. We can observe that the mass function of the FOF halos exhibits a bulge around a mass of 10 particles.

halo classified by different methods. It should be noted that in the first three slices, the CWT halos are also identified as the largest halos. In the final slice, the largest FOF halo corresponds to the second largest CWT halo because it contains a similar number of particles.

In the comparison between CWT and FOF halos, it is observed that CWT halos have fewer particles, are more compact, and are defined by a clearer boundary at grid points where the CWT values are less than zero and decreasing from their local maximum. On the other hand, FOF halos are more diffuse, bounded by voids devoid of particles, and contain more particles. Both FOF and CWT halos feature several density peaks (represented by red particles) and display a multimodal structure indicative of the subhalos within them.

The local density of CWT halos spans approximately two orders of magnitude, slightly less than that of FOF halos, whose local density spans  $\lesssim 3$  orders of magnitude. This discrepancy is due to the no-particle area at the boundaries of FOF halos, which extend at least the linking length. In contrast, the boundary of CWT halos is defined by the change of the density field. As previously mentioned, the CWT of a constant background is zero. Therefore, our CWT halos are delineated solely based on the variation of the density field, resulting in sharp boundaries. This enables us to distinguish between different structures even in highly dense regions, identify each local density peak as a distinct halo, and effectively mitigate the linking bridge problem.

Figure 8 shows that all four CWT halos exclude the outermost layer of their corresponding FOF halos and exhibit a slightly more compact density distribution. The compact shape of the CWT halo is attributed to the boundary condi-

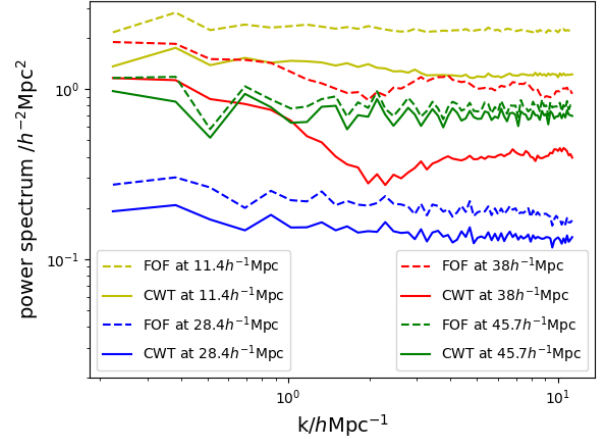


**Figure 12.** Power spectrum of four slices: the solid line represents the power spectrum of the CWT halos, while the dashed line represents that of the FOF halos. It is evident that the CWT halos have a lower power spectrum than their FOF counterparts at all wavenumbers.

tion we use. CWT equals zero means the the convolution of the negative part of wavelet with the central density peak is comparable to the convolution of the positive part of wavelet with outer part of the density peak. The high density peak forces the boundary of CWT equals zero inward to alleviate the the large negative convolution. Consequently, the diffuse and extended outermost parts are not included in the CWT halos. Figure 9 displays the largest FOF halo and its corresponding CWT contours. The scale of the CWT for these contours is set to  $w \sim 4 h\text{Mpc}^{-1}$  for the first two halos and  $w \sim 3 h\text{Mpc}^{-1}$  for the last halo, consistent with the scales of their respective CWT halos.

The contours represent the boundary of the CWT halo with a high enough resolution that cannot be achieved by running the global halo identification program. The CWT halo exhibits a smooth boundary, contrasting with the fractal structure observed in FOF when the resolution is sufficiently high. Additionally, we affirm the importance of introducing our new boundary condition that delineates adjacent structures at the saddle point between them, as depicted in the final image of Figure 9. The large support of the wavelet at a large scale could create a positive bridge linking two adjacent halos if we were to use ‘CWT equals zero’ as the sole boundary condition.

In regions of lower density, the finite resolution no longer poses a problem due to the sharp boundary, as the grid points that constitute the halo already encompass the no-particle voids. This implies that the uniform background density is close to zero in low-density regions. Figure 10 illustrates examples of these CWT halos. Within these halos, the distance between some groups of particles exceeds the linking length, leading to their corresponding FOF halo having fewer parti-

cles or even not forming at all due to an insufficient number of particles. This could partially account for why there are more CWT halos than FOF halos in the medium mass range.

Additionally, the CWT method separates structures based on their CWT values, enabling the identification of relatively weaker and more extended structures within loose regions. These structures, while having a low CWT value, still exceed the threshold and are characterized by a negative ring surrounding them. Consequently, our CWT method can identify these particles as distinct individual halos.

The density distribution of halos can be further examined through the halo mass function depicted in Figure 11. The function indicates that the number of CWT halos exceeds that of FOF halos in the very low mass range (less than 10 particles, near the minimum particle threshold), where CWT has an excess of over 100% in the number of halos. However, as the mass increases to approximately 10 particles, the number of CWT halos abruptly drops to about 40% of FOF. In the higher mass range, the number of CWT halos gradually approaches that of FOF halos and surpasses FOF when the mass reaches around 30 particles. Beyond this point, this excess stabilizes at approximately 20%, with a dispersion of about 20%. In the highest mass range (exceeding 2,000 particles), the scarcity of halo numbers introduces numerous artifacts and inaccuracies. There are even instances where no halos are present across many mass ranges, leading to discontinuities in our halo mass function when plotted on a logarithmic scale.

Overall, all halo mass functions decrease as mass increases, but the CWT function has a smoother shape with no bulge at approximately 10 particles. This function demonstrates high consistency with the scatter observed among those halos where CWT indicates a higher abundance in the intermediate and lower mass ranges.

Finally, we compute the halo power spectrum for four slices by assigning the halos to a  $256^2$  grid using a weighted CIC method. The resulting power spectra are displayed in Figure 12. It is observed that the FOF halo exhibits higher amplitude across all wavenumbers due to containing more particles than the CWT halo. There is a high degree of consistency in the power spectrum across all scales. After a simple translation, the power spectra of the CWT and FOF halos nearly coincide. In summary, the clustering intensity of the CWT halo is similar to, but slightly less than, that of the FOF halo at every scale.

## 6. CONCLUSIONS AND DISCUSSIONS

In this paper, we employ a wavelet-based algorithm to identify halos within pseudo-2D data generated from the SIMBA simulation and compare the results with the traditional FOF method. Our algorithm leverages the ability to discern structures across both space and scale via the CWT,

which can be considered as a ‘mathematical microscope’ for delving into the intricate structure of the density field and automatically extracting its clustering properties. To locate the halos in position-scale space, we initially select a range of scale parameters  $w$  and compute the grid CWT for a series of  $w_i$  within the selected range. We then identify the local maxima of the CWT at each scale and compare them across scales to retain the most prominent maximum at each position. Once all local maxima have been detected, we segment the CWT grid into distinct ‘islands’ to delineate the shape of these local maxima. The ‘islands’ are zoomed and projected back into the simulation space from large scale to small scale, discarding any overlapping islands originating from larger scales. Subsequently, each particle is assessed to ascertain whether it is part of an island. Halo particles are designated, and only halos comprising more than 5 particles are retained.

To prevent the incorrect detection of Poisson noise as halos, we conduct Monte Carlo simulations to assess the significance of each local maximum. We randomly introduce mock particles, equivalent in number to the real data, into the simulation space and determine the detection threshold and its corresponding significance level from the histogram of the CWT values of the mock data. To eliminate the time-consuming aspect of Monte Carlo calculations, we pre-run simulations across a broad range of particle numbers and scales. The outcomes are then fitted to an empirical formula, enabling the establishment of a threshold at the 99.5% significance level with an error margin of approximately 10%. Additionally, the impact of resolution is examined. If the resolution is too low, it becomes challenging to differentiate between closely situated halos, leading to a reduction in the number of detected halos (to two-thirds of the standard resolution). Conversely, doubling the resolution yields a more refined halo boundary, yet it may not accurately reflect the true halo structure because of the shift of its maxima, even though it requires four times the computational resources.

Employing our method, we have successfully compiled a halo catalog. The properties of our CWT halos are compared with those of the FOF halos and are summarized below:

1. The spatial distribution of the CWT halos is similar to that of the FOF halos, and both exhibit a strong correlation with the density field. They demonstrate high number densities in dense regions, show no detection in voids, and even form a web-like structure across all four slices.
2. The CWT method identifies a greater number of halos compared to the FOF method, even though it contains fewer total particles. Specifically, the FOF method accounts for approximately 70% of the total particles, whereas the CWT method includes approximately 10% fewer particles. Furthermore, the CWT

method yields a slightly higher count of halos than the FOF method.

3. The boundary of a CWT halo is delineated by the grid points where the CWT value is less than zero and exhibits a decreasing trend. This boundary serves as a natural demarcation when attempting to partition the entire space into distinct structures. However, owing to our finite grid resolution, the boundary appears comparatively sharp as opposed to the identifications obtained from high-resolution data.
4. Based on the halo mass function, it can be inferred that in the lowest mass range (around 5 particles), the CWT halo exhibits the highest excess in the number of halos, resulting in a finer shape of its mass function. After the bulge of the FOF halo mass function, the number of CWT halos gradually increases to match that of the FOF and ultimately stabilizes at an excess of approximately 20%.
5. Despite having a lower amplitude, the halo power spectrum of the CWT halos is consistent with that of the FOF halos across all scales. This suggests that, although the clustering intensity of the CWT halos is weaker than that of the FOF halos, the trends they follow are similar.

Overall, our findings indicate that the CWT is capable of identifying halos in cosmological simulations, owing to its high consistency with the identification results of the FOF method. The aim of this paper is to demonstrate the feasibility of our CWT approach. It should be noted that there is significant potential for improvement in both our program and algorithm, as discussed in Appendix A. Additionally, our algorithm relies solely on the positional data of these particles. To ascertain that any group of particles constitutes a halo that more closely resembles reality, we require the complete dynamic information of the particles. This is because dark matter halos are gravity-bound, virialized structures. Consequently, in future work, we will incorporate the velocity information of particles to achieve a more accurate represen-

tation of the dynamical structure of our CWT-identified halos.

In the current work, we chose to work with 2D rather than 3D data for several reasons as follows. (1) Compared with the 3D case, halos identified with 2D data can be completed with lower costs in processing time, memory and storage space, making the development and testing of algorithms more efficient. (2) Working in the 2D case can simplify the problem, allowing us to more easily identify and address issues without the added complexity of an additional dimension. (3) 2D data is easier to visualize, which is very helpful for demonstrating and understanding the effects of an algorithm. (4) Working in the 2D case can serve as an intermediate step towards transitioning to the 3D case; the concept can first be proven in 2D before extending the research to 3D case. Despite these benefits, our 2D test is not yet practical for real-world applications, given that we inhabit a 3D universe. To develop a program capable of analyzing real data rather than pseudo-2D data, we must account for the 3D case and optimize our program for enhanced performance.

Currently, the performance of our program results in unacceptable time costs when processing significantly larger datasets in the 3D context, so we particularly need a fast wavelet algorithm for 3D particle data (e.g. Romeo et al. 2008; Wang & He 2023), which will be the target of our next study. Furthermore, the capability to discern structures across scales using CWT holds the potential to detect sub-structures within the CWT halo, which may also be explored in our future research.

## ACKNOWLEDGMENTS

MXL thanks Prof. Pin Lyu for his assistance with some numerical techniques. The authors also express their gratitude to the SIMBA team for making their data publicly available.

*Software:* NumPy (<https://numpy.org/>), SciPy (<https://scipy.org/>), Matplotlib (<https://matplotlib.org/>), Jupyter Notebook (<https://jupyter.org/>), yt project (<https://github.com/yt-project>)

## APPENDIX

### A. PERFORMANCE EVALUATION OF THE CWT METHOD

To properly evaluate the performance of an algorithm, it is crucial to understand its actual capabilities. In the case of our CWT method, we conducted tests to measure the time required for calculating data of varying sizes. We select slices with thicknesses ranging from  $0.02 h^{-1}\text{Mpc}$  to  $0.5 h^{-1}\text{Mpc}$  to generate test pseudo-2D data, which we then use to run

our halo identification program. The tests are conducted on a platform equipped with an AMD Ryzen 9 7900X CPU and 64GB of DDR5 6000MHz RAM.

The program consists of two components: calculating grid CWT and characterizing local maxima. We test the time costs for each part separately and compare them with those of the FOF method. The results are depicted in Figure A1. Both the FOF method, as calculated by yt-project, and our

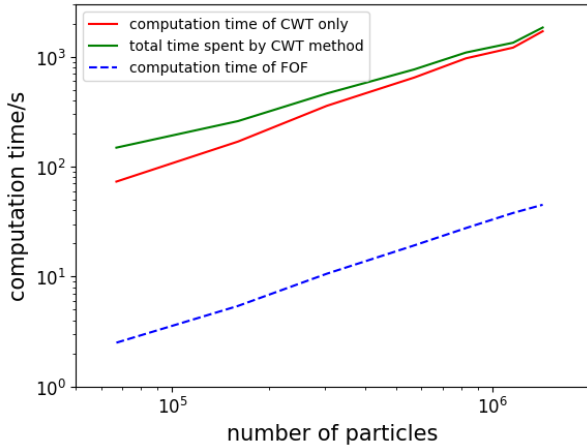


**Figure A1.** The computation time varies with different data sizes, ranging from 66,942 to 1,435,111 (which corresponds to a thickness from  $0.02 h^{-1}\text{Mpc}$  to  $0.5 h^{-1}\text{Mpc}$ ). The blue dashed line represents the computation time for the FOF method, and the solid line represents that for the CWT method. The  $\mathcal{O}(N \log N)$  time complexity for FOF method exhibits as linear in this log-log plot.

CWT method exhibit linear time complexity in our tests. The time cost for the former part of our program (represented by the red line) increases linearly with data size, while the latter part demonstrates significantly less variation. This is because, even with fewer particles in the thinnest slice, the number of local maxima does not change rapidly. The slice at  $0.02 h^{-1}\text{Mpc}$  contains 2,481 local maxima, and concurrently, the thickest slice at  $0.5 h^{-1}\text{Mpc}$  contains only 4,270, hence the time required to characterize them varies correspondingly slowly.

The performance of our program is significantly inferior to that of YT. We spend 60 times as much time on the smallest data set and 40 times as much on the largest data set. However, it is not advisable to compare the performance of a test program directly with that of a well-optimized project. Therefore, our primary goal is to confirm the  $\mathcal{O}(N)$  time complexity of our program.

## REFERENCES

- Arnalte-Mur, P., Labatie, A., Clerc, N., et al. 2012, *A&A*, 542, A34, doi: [10.1051/0004-6361/201118017](https://doi.org/10.1051/0004-6361/201118017)
- Baluev, R. V., & Rodionov, E. I. 2020, *Celestial Mechanics and Dynamical Astronomy*, 132, 34, doi: [10.1007/s10569-020-09976-2](https://doi.org/10.1007/s10569-020-09976-2)
- Barnard, V. E., Vielva, P., Pierce-Price, D. P. I., et al. 2004, *MNRAS*, 352, 961, doi: [10.1111/j.1365-2966.2004.07985.x](https://doi.org/10.1111/j.1365-2966.2004.07985.x)
- Behroozi, P. S., Wechsler, R. H., & Wu, H.-Y. 2013, *ApJ*, 762, 109, doi: [10.1088/0004-637X/762/2/109](https://doi.org/10.1088/0004-637X/762/2/109)
- Bendjoya, P., Slezak, E., & Froeschle, C. 1991, *A&A*, 251, 312
- Bijaoui, A., & Giudicelli, M. 1990, *Experimental Astronomy*, 1, 347, doi: [10.1007/BF00426718](https://doi.org/10.1007/BF00426718)
- Bijaoui, A., Slezak, E., & Mars, G. 1992, in *Distribution of Matter in the Universe*, ed. G. A. Mamon & D. Gerbal, 323–332
- Cayón, L., Sanz, J. L., Barreiro, R. B., et al. 2000, *MNRAS*, 315, 757, doi: [10.1046/j.1365-8711.2000.03462.x](https://doi.org/10.1046/j.1365-8711.2000.03462.x)
- Chereul, E., Creze, M., & Bienayme, O. 1998, *A&A*, 340, 384, doi: [10.48550/arXiv.astro-ph/9809263](https://doi.org/10.48550/arXiv.astro-ph/9809263)
- Ciprini, S., Tosti, G., Marcucci, F., et al. 2007, in *American Institute of Physics Conference Series*, Vol. 921, *The First GLAST Symposium*, ed. S. Ritz, P. Michelson, & C. A. Meegan, 546–547
- Daubechies, I. 1992, *Ten lectures on wavelets* (Philadelphia, PA: SIAM)
- Davé, R., Anglés-Alcázar, D., Narayanan, D., et al. 2019, *MNRAS*, 486, 2827, doi: [10.1093/mnras/stz937](https://doi.org/10.1093/mnras/stz937)
- Davis, M., Efstathiou, G., Frenk, C. S., & White, S. D. M. 1985, *ApJ*, 292, 371, doi: [10.1086/163168](https://doi.org/10.1086/163168)
- Djafer, D., Irbah, A., & Meftah, M. 2012, *SoPh*, 281, 863, doi: [10.1007/s11207-012-0109-3](https://doi.org/10.1007/s11207-012-0109-3)
- Einasto, J., Hütsi, G., Saar, E., et al. 2011, *A&A*, 531, A75, doi: [10.1051/0004-6361/201016070](https://doi.org/10.1051/0004-6361/201016070)
- Ellien, A., Slezak, E., Martinet, N., et al. 2021, *A&A*, 649, A38, doi: [10.1051/0004-6361/202038419](https://doi.org/10.1051/0004-6361/202038419)
- Escalera, E., Biviano, A., Girardi, M., et al. 1994, *ApJ*, 423, 539, doi: [10.1086/173833](https://doi.org/10.1086/173833)
- Flin, P., & Krywult, J. 2006, *A&A*, 450, 9, doi: [10.1051/0004-6361:20041635](https://doi.org/10.1051/0004-6361:20041635)
- Freeman, P. E., Kashyap, V., Rosner, R., & Lamb, D. Q. 2002, *ApJS*, 138, 185, doi: [10.1086/324017](https://doi.org/10.1086/324017)
- González-Gómez, D. I., Blanco-Cano, X., & Raga, A. C. 2010, *Advances in Space Research*, 46, 22, doi: [10.1016/j.asr.2010.02.022](https://doi.org/10.1016/j.asr.2010.02.022)
- Grebenev, S. A., Forman, W., Jones, C., & Murray, S. 1995, *ApJ*, 445, 607, doi: [10.1086/175725](https://doi.org/10.1086/175725)
- Grossmann, A., Morlet, J., & Paul, T. 1985, *Journal of Mathematical Physics*, 26, 2473, doi: [10.1063/1.526761](https://doi.org/10.1063/1.526761)
- Hayn, M., Panet, I., Diament, M., et al. 2012, *Geophysical Journal International*, 189, 1430, doi: [10.1111/j.1365-246X.2012.05455.x](https://doi.org/10.1111/j.1365-246X.2012.05455.x)
- Hockney, R. W., & Eastwood, J. W. 1981, *Computer Simulation Using Particles* (New York: McGraw-Hill)
- Hopkins, P. F. 2015, *MNRAS*, 450, 53, doi: [10.1093/mnras/stv195](https://doi.org/10.1093/mnras/stv195)

- Kazakevich, E., Vityazev, V., & Orlov, V. 2004, in *Astronomical Society of the Pacific Conference Series*, Vol. 316, *Order and Chaos in Stellar and Planetary Systems*, ed. G. G. Byrd, K. V. Kholshchevnikov, A. A. Myllri, I. I. Nikiforov, & V. V. Orlov, 243
- Knollmann, S. R., & Knebe, A. 2009, *ApJS*, 182, 608, doi: [10.1088/0067-0049/182/2/608](https://doi.org/10.1088/0067-0049/182/2/608)
- Lazzati, D., Campana, S., Rosati, P., Panzera, M. R., & Tagliaferri, G. 1999, *ApJ*, 524, 414, doi: [10.1086/307788](https://doi.org/10.1086/307788)
- Mertens, F., & Lobanov, A. 2015, *A&A*, 574, A67, doi: [10.1051/0004-6361/201424566](https://doi.org/10.1051/0004-6361/201424566)
- Mo, H., van den Bosch, F., & White, S. 2010, *Galaxy Formation and Evolution* (Cambridge University Press), doi: [10.1017/CBO9780511807244](https://doi.org/10.1017/CBO9780511807244)
- More, S., Kravtsov, A. V., Dalal, N., & Gottlöber, S. 2011, *ApJS*, 195, 4, doi: [10.1088/0067-0049/195/1/4](https://doi.org/10.1088/0067-0049/195/1/4)
- Moretti, A., Guzzo, L., Campana, S., et al. 2004, *A&A*, 428, 21, doi: [10.1051/0004-6361:20041326](https://doi.org/10.1051/0004-6361:20041326)
- Nelson, D., Springel, V., Pillepich, A., et al. 2019, *Computational Astrophysics and Cosmology*, 6, 2, doi: [10.1186/s40668-019-0028-x](https://doi.org/10.1186/s40668-019-0028-x)
- Pagliaro, A., Antonuccio-Delogu, V., Becciani, U., & Gambera, M. 1999, *MNRAS*, 310, 835, doi: [10.1046/j.1365-8711.1999.02995.x](https://doi.org/10.1046/j.1365-8711.1999.02995.x)
- Patrikeev, I., Fletcher, A., Stepanov, R., et al. 2006, *A&A*, 458, 441, doi: [10.1051/0004-6361:20065225](https://doi.org/10.1051/0004-6361:20065225)
- Peebles, P. 1980, *The Large-scale Structure of the Universe*, Princeton Series in Physics (Princeton University Press)
- Planck Collaboration, Ade, P. A. R., Aghanim, N., et al. 2016, *A&A*, 594, A13, doi: [10.1051/0004-6361/201525830](https://doi.org/10.1051/0004-6361/201525830)
- Planelles, S., & Quilis, V. 2010, *A&A*, 519, A94, doi: [10.1051/0004-6361/201014214](https://doi.org/10.1051/0004-6361/201014214)
- Press, W. H., & Schechter, P. 1974, *ApJ*, 187, 425, doi: [10.1086/152650](https://doi.org/10.1086/152650)
- Romeo, A. B., Agertz, O., Moore, B., & Stadel, J. 2008, *ApJ*, 686, 1, doi: [10.1086/591236](https://doi.org/10.1086/591236)
- Slezak, E., Bijaoui, A., & Mars, G. 1990, *A&A*, 227, 301
- Slezak, E., de Lapparent, V., & Bijaoui, A. 1993, *ApJ*, 409, 517, doi: [10.1086/172683](https://doi.org/10.1086/172683)
- Springel, V., White, S. D. M., Tormen, G., & Kauffmann, G. 2001, *MNRAS*, 328, 726, doi: [10.1046/j.1365-8711.2001.04912.x](https://doi.org/10.1046/j.1365-8711.2001.04912.x)
- Turk, M. J., Smith, B. D., Oishi, J. S., et al. 2011, *ApJS*, 192, 9, doi: [10.1088/0067-0049/192/1/9](https://doi.org/10.1088/0067-0049/192/1/9)
- Vavilova, I. B., & Babyk, I. V. 2018, *Odessa Astronomical Publications*, 30, 239, doi: [10.18524/1810-4215.2018.31.146678](https://doi.org/10.18524/1810-4215.2018.31.146678)
- Wang, L., Rowan-Robinson, M., Yamamura, I., et al. 2008, *MNRAS*, 387, 601, doi: [10.1111/j.1365-2966.2008.13292.x](https://doi.org/10.1111/j.1365-2966.2008.13292.x)
- Wang, Y., & He, P. 2021, *Communications in Theoretical Physics*, 73, 095402, doi: [10.1088/1572-9494/ac10be](https://doi.org/10.1088/1572-9494/ac10be)
- . 2022, *ApJ*, 934, 112, doi: [10.3847/1538-4357/ac7a3d](https://doi.org/10.3847/1538-4357/ac7a3d)
- Wang, Y., & He, P. 2023, *RAS Techniques and Instruments*, 2, 307, doi: [10.1093/rasti/rzad020](https://doi.org/10.1093/rasti/rzad020)
- Wang, Y., Yang, H.-Y., & He, P. 2022, *ApJ*, 934, 77, doi: [10.3847/1538-4357/ac752c](https://doi.org/10.3847/1538-4357/ac752c)